

Measurement of the Atmospheric Muon Charge Ratio at TeV Energies with MINOS

P. Adamson,^{1,2} C. Andreopoulos,³ K. E. Arms,⁴ R. Armstrong,⁵ D. J. Auty,⁶ S. Avvakumov,⁷ D. S. Ayres,⁸ B. Baller,¹ B. Barish,⁹ P. D. Barnes Jr.,¹⁰ G. Barr,¹¹ W. L. Barrett,¹² E. Beall,^{8,4,*} B. R. Becker,⁴ A. Belias,³ T. Bergfeld,^{13,†} R. H. Bernstein,¹ D. Bhattacharya,¹⁴ M. Bishai,¹⁵ A. Blake,¹⁶ B. Bock,¹⁷ G. J. Bock,¹ J. Boehm,¹⁸ D. J. Boehnlein,¹ D. Bogert,¹ P. M. Border,⁴ C. Bower,⁵ E. Buckley-Geer,¹ C. Bungau,⁶ A. Cabrera,^{11,‡} J. D. Chapman,¹⁶ D. Cherdack,¹⁹ S. Childress,¹ B. C. Choudhary,¹ J. H. Cobb,¹¹ A. J. Culling,¹⁶ J. K. de Jong,²⁰ A. De Santo,^{11,§} M. Dierckxsens,¹⁵ M. V. Diwan,¹⁵ M. Dorman,^{2,3} D. Drakoulakos,²¹ T. Durkin,³ A. R. Erwin,²² C. O. Escobar,²³ J. J. Evans,¹¹ E. Falk Harris,⁶ G. J. Feldman,¹⁸ T. H. Fields,⁸ R. Ford,¹ M. V. Frohne,^{24,¶} H. R. Gallagher,¹⁹ G. A. Giurgiu,⁸ A. Godley,¹³ J. Gogos,⁴ M. C. Goodman,⁸ P. Gouffon,²⁵ R. Gran,¹⁷ E. W. Grashorn,^{4,17} N. Grossman,¹ K. Grzelak,¹¹ A. Habig,¹⁷ D. Harris,¹ P. G. Harris,⁶ J. Hartnell,³ E. P. Hartouni,¹⁰ R. Hatcher,¹ K. Heller,⁴ A. Holin,² C. Howcroft,⁹ J. Hysten,¹ D. Indurthy,²⁶ G. M. Irwin,⁷ M. Ishitsuka,⁵ D. E. Jaffe,¹⁵ C. James,¹ L. Jenner,² D. Jensen,¹ T. Joffe-Minor,⁸ T. Kafka,¹⁹ H. J. Kang,⁷ S. M. S. Kasahara,⁴ M. S. Kim,¹⁴ G. Koizumi,¹ S. Kopp,²⁶ M. Kordosky,² D. J. Koskinen,² S. K. Kotelnikov,²⁷ A. Kreymer,¹ S. Kumaratunga,⁴ K. Lang,²⁶ A. Lebedev,¹⁸ R. Lee,^{18,**} J. Ling,¹³ J. Liu,²⁶ P. J. Litchfield,⁴ R. P. Litchfield,¹¹ P. Lucas,¹ W. A. Mann,¹⁹ A. Marchionni,¹ A. D. Marino,¹ M. L. Marshak,⁴ J. S. Marshall,¹⁶ N. Mayer,¹⁷ A. M. McGowan,^{8,4} J. R. Meier,⁴ G. I. Merzon,²⁷ M. D. Messier,⁵ D. G. Michael,^{9,††} R. H. Milburn,¹⁹ J. L. Miller,^{28,††} W. H. Miller,⁴ S. R. Mishra,¹³ A. Mislivec,¹⁷ P. S. Miyagawa,¹¹ C. D. Moore,¹ J. Morfín,¹ L. Mualem,⁴ S. Mufson,⁵ S. Murgia,⁷ J. Musser,⁵ D. Naples,¹⁴ J. K. Nelson,²⁹ H. B. Newman,⁹ R. J. Nichol,^{2,‡‡} T. C. Nicholls,³ J. P. Ochoa-Ricoux,⁹ W. P. Oliver,¹⁹ T. Osiecki,²⁶ R. Ospanov,²⁶ J. Paley,⁵ V. Paolone,¹⁴ A. Para,¹ T. Patzak,³⁰ Ž. Pavlović,²⁶ G. F. Pearce,³ C. W. Peck,⁹ E. A. Peterson,⁴ D. A. Petyt,⁴ H. Ping,²² R. Piteira,³⁰ R. Pittam,¹¹ R. K. Plunkett,¹ D. Rahman,⁴ R. A. Rameika,¹ T. M. Raufer,¹¹ B. Rebel,¹ J. Reichenbacher,⁸ D. E. Reyna,⁸ C. Rosenfeld,¹³ H. A. Rubin,²⁰ K. Ruddick,⁴ V. A. Ryabov,²⁷ R. Saakyan,² M. C. Sanchez,¹⁸ N. Saoulidou,¹ J. Schneps,¹⁹ P. Schreiner,²⁴ V. K. Semenov,³¹ S.-M. Seun,¹⁸ P. Shanahan,¹ W. Smart,¹ V. Smirnitsky,³² C. Smith,^{2,6} A. Sousa,^{11,19} B. Speakman,⁴ P. Stamoulis,²¹ P. A. Symes,⁶ N. Tagg,^{19,11} R. L. Talaga,⁸ E. Tetteh-Lartey,³³ J. Thomas,² J. Thompson,^{14,††} M. A. Thomson,¹⁶ J. L. Thron,^{8,§§} G. Tinti,¹¹ I. Trostin,³² V. A. Tsarev,²⁷ G. Tzanakos,²¹ J. Urheim,⁵ P. Vahle,² C. Velissaris,²² V. Verebryusov,³² B. Viren,¹⁵ C. P. Ward,¹⁶ D. R. Ward,¹⁶ M. Watabe,³³ A. Weber,^{11,3} R. C. Webb,³³ A. Wehmann,¹ N. West,¹¹ C. White,²⁰ S. G. Wojcicki,⁷ D. M. Wright,¹⁰ Q. K. Wu,¹³ T. Yang,⁷ F. X. Yumiceva,²⁹ H. Zheng,⁹ M. Zois,²¹ and R. Zwaska^{1,26}

(The MINOS Collaboration)

¹Fermi National Accelerator Laboratory, Batavia, IL 60510

²Dept. of Physics and Astronomy, University College London, Gower Street, London WC1E 6BT, UK

³Rutherford Appleton Laboratory, Chilton, Didcot, Oxfordshire, OX11 0QX, UK

⁴University of Minnesota, Minneapolis, MN 55455

⁵Departments of Physics and Astronomy, Indiana University, Bloomington, IN 47405

⁶Dept. of Physics and Astronomy, University of Sussex, Falmer, Brighton BN1 9QH, UK

⁷Department of Physics, Stanford University, Stanford, CA 94305

⁸Argonne National Laboratory, Argonne, IL 60439

⁹Lauritsen Lab, California Institute of Technology, Pasadena, CA 91125

¹⁰Lawrence Livermore National Laboratory, Livermore, CA 94550

¹¹Sub-dept. of Particle Physics, Univ. of Oxford, Denys Wilkinson Bldg, Keble Road, Oxford OX1 3RH, UK

¹²Physics Dept., Western Washington Univ., Bellingham, WA 98225

¹³Dept. of Physics and Astronomy, Univ. of South Carolina, Columbia, SC 29208

¹⁴Dept. of Physics and Astronomy, Univ. of Pittsburgh, Pittsburgh, PA 15260

¹⁵Brookhaven National Laboratory, Upton, NY 11973

¹⁶Cavendish Laboratory, Univ. of Cambridge, Madingley Road, Cambridge CB3 0HE, UK

¹⁷Dept. of Physics, Univ. of Minnesota – Duluth, Duluth, MN 55812

¹⁸High Energy Physics Lab, Harvard University, Cambridge, MA 02138

¹⁹Physics Dept., Tufts University, Medford, MA 02155

²⁰Physics Division, Illinois Institute of Technology, Chicago, IL 60616

²¹Department of Physics, University of Athens, GR-15771 Athens, Greece

²²Physics Dept., Univ. of Wisconsin, Madison, WI 53706

²³Univ. Estadual de Campinas, IF-UNICAMP, CP 6165, 13083-970, Campinas, SP, Brazil

²⁴Physics Dept., Benedictine University, Lisle, IL 60532

²⁵Inst. de Física, Univ. de São Paulo, CP 66318, 05315-970, São Paulo, SP, Brazil

²⁶Dept. of Physics, Univ. of Texas, 1 University Station, Austin, TX 78712

²⁷Nuclear Physics Dept., Lebedev Physical Inst., Leninsky Prospect 53, 117924 Moscow, Russia

²⁸Physics Dept., James Madison University, Harrisonburg, VA 22807

²⁹*Dept. of Physics, College of William & Mary, Williamsburg, VA 23187*

³⁰*APC – Collège de France, 11 Place Marcelin Berthelot, F-75231 Paris Cedex 05, France*

³¹*Inst. for High Energy Physics, Protvino, Moscow Region RU-140284, Russia*

³²*High Energy Exp. Physics Dept., Inst. of Theor. and Exp. Physics, B. Cheremushkinskaya, 25, 117218 Moscow, Russia*

³³*Physics Dept., Texas A&M Univ., College Station, TX 77843*

(Dated: May 25, 2007)

The 5.4 kton MINOS far detector has been taking charge-separated cosmic ray muon data since the beginning of August, 2003 at a depth of 2070 meters-water-equivalent in the Soudan Underground Laboratory, Minnesota, USA. The data with both forward and reversed magnetic field running configurations were combined to minimize systematic errors in the determination of the underground muon charge ratio. When averaged, two independent analyses find the charge ratio underground to be

$$N_{\mu^+}/N_{\mu^-} = 1.374 \pm 0.004 \text{ (stat.)}_{-0.010}^{+0.012} \text{ (sys.)}.$$

Using the map of the Soudan rock overburden, the muon momenta as measured underground were projected to the corresponding values at the surface in the energy range 1-7 TeV. Within this range of energies at the surface, the MINOS data are consistent with the charge ratio being energy independent at the two standard deviation level. When the MINOS results are compared with measurements at lower energies, a clear rise in the charge ratio in the energy range 0.3 – 1.0 TeV is apparent. A qualitative model shows that the rise is consistent with an increasing contribution of kaon decays to the muon charge ratio.

PACS numbers:

I. INTRODUCTION

The MINOS far detector is a 5.4 kton calorimeter, with magnetized steel planes located at the Soudan Underground Laboratory, Minnesota, USA. It was designed to study neutrino oscillations with the NuMI beam which originates 735 km away at Fermilab. At a depth of 710 meters below the Earth's surface, the MINOS far detector is the deepest experiment to measure cosmic ray muons with a magnetized detector, thus providing a capability to distinguish μ^+ from μ^- with large statistics. The data correspond to muon energies at the surface in excess of approximately 1 TeV. Above this energy, there are few measurements of the charge ratio N_{μ^+}/N_{μ^-} .

Cosmic ray muons are produced when primary cosmic ray nuclei, mostly single protons, interact at the top of the atmosphere to produce hadronic showers. The pions and kaons in these showers decay to muons, which are measured in detectors on the surface and underground, and with balloon-borne experiments in the atmosphere. Since the cosmic ray primaries are positively charged,

there are more positive than negative pions and kaons in the resulting hadronic showers. In the energy range from 3 to 100 GeV, the CORT (Cosmic-Origin Radiation Transport) cosmic ray Monte Carlo [1] predicts a relatively constant charge ratio of $N_{\mu^+}/N_{\mu^-} \approx 1.3$. In a compilation of measurements, the charge ratio was approximately constant at $N_{\mu^+}/N_{\mu^-} \approx 1.27$ with uncertainties increasing from $\sim 1\%$ at a few hundred MeV to $\sim 6\%$ at 300 GeV [2]. A more recent measurement by the L3+C experiment at CERN found similar results in the range 20 - 500 GeV [3].

At energies greater than a few hundred GeV, several competing processes can affect the charge ratio. The muons seen by MINOS result from pions and kaons that decay before they interact in the atmosphere. As energy increases, the fraction of muons seen from kaon decays also increases because the longer-lived pions have become more likely to interact before decaying than the shorter-lived kaons. Consequently, kaon decays begin to make an increasingly more important contribution to the muon charge ratio at these energies. Since strong interaction production channels lead to a muon charge ratio from kaon decays that is greater than that from pion decays, the measured charge ratio is expected to increase. Several competing processes, however, could counter this increase at even higher energies. Decays of charmed hadrons are one such process. There is also the possibility that heavier elements become a more important component of cosmic ray primaries as the energy increases. This increasingly heavy composition would decrease the ratio of primary protons to neutrons, thereby decreasing the muon charge ratio. With careful measurements of the N_{μ^+}/N_{μ^-} ratio in the cosmic rays, models of the interactions of cosmic rays in the atmosphere can be improved.

In addition, measurements of the cosmic ray muon

*Now at Cleveland Clinic, Cleveland, OH 44195.

†Now at GE Healthcare, Florence SC 29501.

‡Now at APC – Collège de France, 11 Place Marcelin Berthelot, F-75231 Paris Cedex 05, France.

§Now at Physics Dept., Royal Holloway, Univ. of London, Egham, Surrey, TW20 0EX, UK.

¶Now at Holy Cross College, Notre Dame, IN 46556.

**Now at Lincoln Laboratory, Massachusetts Institute of Technology, Lexington, MA 02420.

††Deceased.

‡‡Now at Dept. of Physics, Pennsylvania State Univ., University Park, PA 16802.

§§Now at Nucl. Nonprolif. Div., Threat Reduc. Dir., Los Alamos National Laboratory, Los Alamos, NM 87545.

charge ratio from a few GeV to a few TeV are important to constrain calculations of the atmospheric neutrino fluxes. These are of interest both for detailed measurements of neutrino oscillations in atmospheric neutrino experiments and also for calculations of backgrounds for neutrino telescopes. The muon charge ratio is a particularly useful tool for testing the predicted atmospheric $\bar{\nu}/\nu$ ratio [1, 4, 5].

In MINOS, underground charge-separated cosmic muons were first studied in detail by Rebel [6] and Beall [7].

II. THE MINOS FAR DETECTOR

The MINOS far detector is a steel-scintillator sampling and tracking calorimeter located at a depth of 2070 meters-water-equivalent (m.w.e.) in the Soudan Underground Laboratory in an iron mine in northern Minnesota (47.82027° N latitude, and 92.24141° W longitude)[8]. The detector is made of 486 octagonal planes of 2.54 cm thick steel laminates, interleaved with 484 planes of 1 cm thick extruded polystyrene scintillator strips at a 5.94 cm pitch. Each scintillator plane has 192 strips of width 4.1 cm. The length of each strip depends on its position in the plane and varies between 3.4–8.0 m. The scintillator strips in alternating detector planes are oriented at $\pm 45^\circ$ to the vertical. The modular detector consists of two supermodules (SM) separated by a gap of 1.1 m. Fig. 1 shows the coordinate system used in the MINOS far detector cosmic ray analysis. In terms of this coordinate system, events are described as coming from the zenith angle θ (the polar angle measured from the y -axis) from vertical ($\theta = 0^\circ$) toward the horizon ($\theta = 90^\circ$), and the azimuthal angle ϕ measured in the $x - z$ plane from true north ($\phi = 0^\circ$) to the east ($\phi = 90^\circ$).

Light from charged particles traversing the MINOS plastic scintillator is collected with wavelength shifting (WLS) plastic fibers embedded within the scintillator strips. The WLS fibers are coupled to clear optical fibers at both ends of a strip and are read out using 16-pixel multi-anode photomultiplier tubes (PMTs). The signals from eight strips, each one of which is separated by approximately 1 m within the same plane, are optically summed and read out by a single PMT pixel. The fibers summed on each pixel are different for the two sides of the detector, which enables the resulting eightfold ambiguity to be resolved for single particle events. For all other types of events, ambiguities are effectively resolved using additional information from timing and event topology.

The data acquisition and trigger have been described in [9]. The primary trigger requires activity to be observed on 4 planes out of 5 within 156 ns. The detector calibration has been described in [10]. More detailed detector information can be found in [8].

In order to measure the momentum of muons traversing the detector, the steel has been magnetized into a toroidal field configuration. A finite element analysis cal-

culuation of the magnetic field strength for a typical MINOS detector plane is shown in Fig. 2. These calculations show that each SM is magnetized to an average value of 1.3 T by the 15 kA current loop that runs through the coil hole (c.f., Fig. 1) along the detector’s z -axis. The field is saturated near the coil hole at a strength of approximately 1.8 T, falling to almost 1 T near the edges. There are small variations in field strength near the corners and along the gaps between the eight plates that make up each steel plane. The detector field was designed to bend or ‘focus’ negatively charged muons travelling from detector South (i.e., μ^- resulting from ν_μ interactions in the detector from neutrinos originating in the Fermilab NuMI beam) toward the center of the detector.

The toroidal magnetic field of the MINOS far detector impacts the acceptance of μ^- and μ^+ entering the detector as a function of their incoming trajectories and the field direction. A muon is “focused” when the magnetic field steers it toward the center of the detector and “defocused” when directed away from the center. These effects are most apparent for muons with trajectories that are parallel to the detector z axis. In one field orientation, Forward Field running, μ^- which enter the detector from the south and the μ^+ which enter from the north will be focused into the center of the detector, while the muons in the opposite charge sign and trajectory combinations will be defocused. Forward Field running (“DF” – data forward) is the default configuration for MINOS data-taking with the NuMI beam from Fermilab. MINOS has a second field orientation, Reverse Field running (“DR” – data reverse), in which the coil current is reversed and μ^+ from the south are focused into the detector. These focusing/defocusing effects are most important at the edges of the detector acceptance and as a result, the charge ratio for muons with incoming trajectories on the edges of the detector acceptance will be either enhanced or suppressed depending on the charge and incoming direction of the muons.

III. DATA ANALYSIS

A. Cosmic Muon Data Sample

In this paper we present results from data recorded between August 1, 2003 and February 28, 2006. During this period, the detector ran with both the DF and DR magnetic field configurations. There were 609.82 live days of Forward Field running and 201.75 live days of Reverse Field running. There were 28,994,380 events in the DF sample and 8,898,551 events in the DR sample.

B. Simulated Cosmic Muons

We generated a sample of 1.2×10^6 cosmic muons by Monte Carlo (“MC”) simulation. Each event was generated by first choosing an arrival direction from the zenith

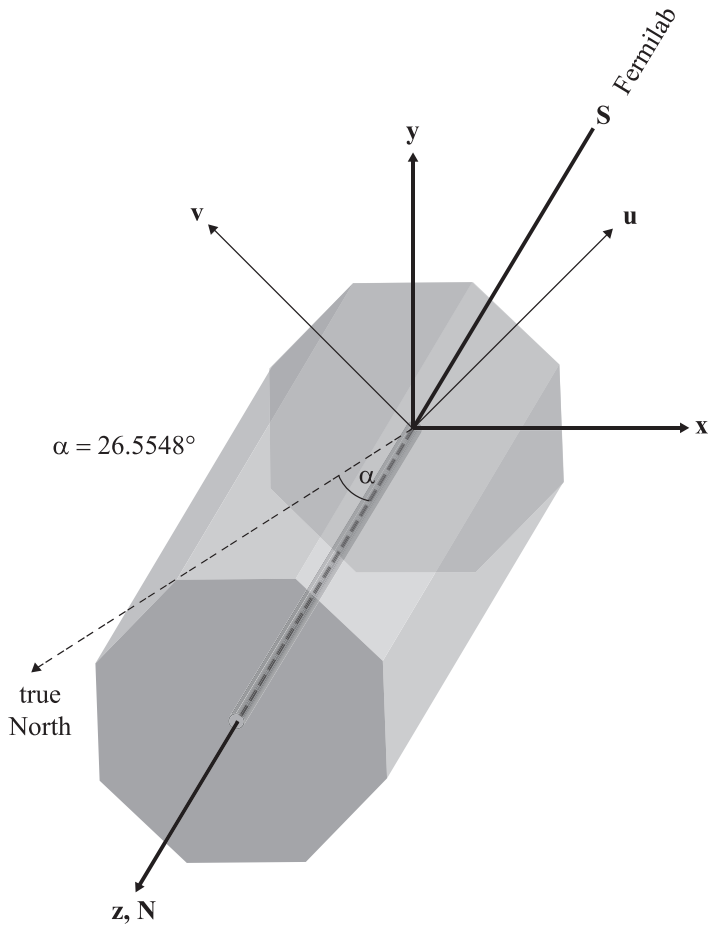


FIG. 1: The coordinate system for the MINOS cosmic ray analysis. The octagonal steel and scintillator planes of the MINOS far detector are 8 m across. The detector is 30 m long. The central hole is for the magnet coil. The $+z$ -axis is along the long axis of the detector and points toward detector North (N). Detector South (S) points back towards Fermilab. The y -axis is directed toward the zenith. The x -axis direction is chosen to make a right-handed coordinate system. The origin of the coordinate system is the center of the South face of the detector. Detector North (N) is rotated from true North by an angle $\alpha = 26.5548^\circ$ about the y -axis as measured by a gyro-theodolite; detector North therefore points along an azimuthal angle of 333.4452° . Alternating planes of scintillator strips are oriented along either the u or v axis directions, a coordinate system in which the $x-y$ plane is rotated by $+45^\circ$ about the z -axis.

angle dependence of the muon flux parameterization on the surface [11] and then associating this direction with the overburden [g/cm^2] in the Soudan 2 slant depth map [12]. The energy of the event was selected from the surface cosmic ray muon distribution [11]. With the energy and overburden, the event was tested to see whether it penetrated to the detector [13]. The events that survived were placed on an imaginary box positioned around the detector [14] and then propagated through the detector with the GEANT3 simulation of the MINOS detector.

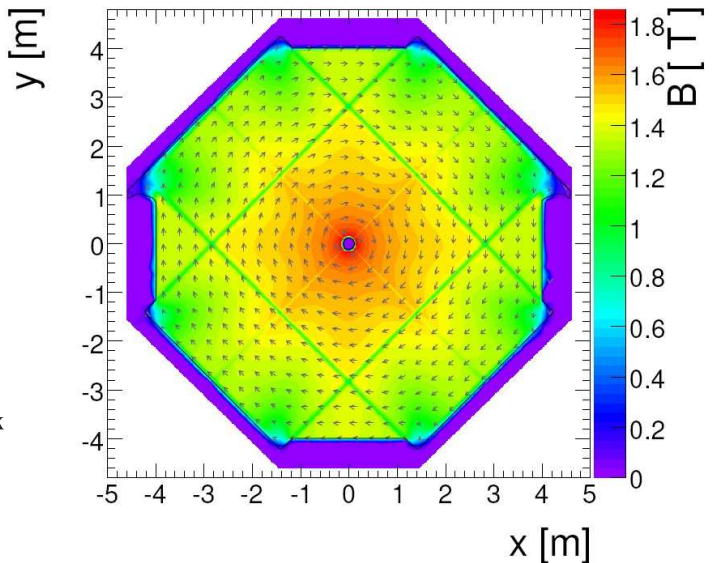


FIG. 2: Finite element analysis model for the toroidal magnetic field in a plane of MINOS steel. The coordinate system for the field map is shown in Fig. 1. In this map, the detector plane is being viewed from detector North.

C. Event Selection

The first stage of the event selection is to identify and remove periods of data associated with detector hardware problems. The criteria defining bad runs are described in [15]. The sample was selected using a series of cuts that were used for both data and MC. The cuts used are described in detail below and the numbers of events remaining at each stage in the selection are listed in Table I.

1. Pre-Analysis Cuts

The first cut in the event selection requires at least one reconstructed track in the event (“1. no reconstruction”). This requirement predominantly removes noise where the primary trigger was satisfied, but there was not enough activity to resolve the eightfold ambiguity from the optical summing of the scintillator strips. The second requires that there is only a single track found by the track-fitting algorithm (“2. multiples cut”). The third requires that the coil be on and in a known state (“3. coil status cut”).

2. Analysis Cuts

The next set of cuts are meant to separate muon tracks from the background with high reliability. These cuts require that: a track must cross at least 20 planes in the detector (“1. 20 plane cut”); a track must have a path length of at least 2 m (“2. 2.0 m track length cut”); the

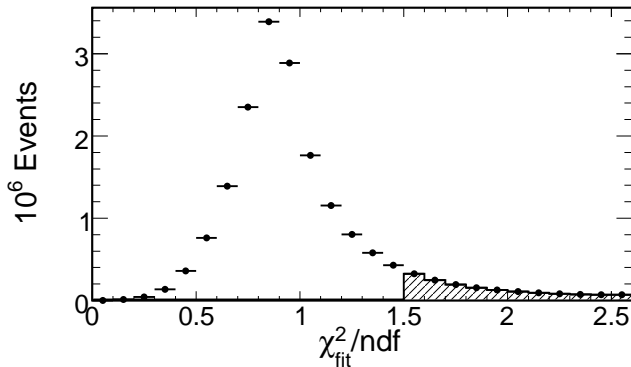


FIG. 3: Distribution of χ_{fit}^2/ndf for the fits to cosmic muon tracks. The cut was made at $\chi_{fit}^2/ndf > 1.5$. The shaded region shows the excluded tracks.

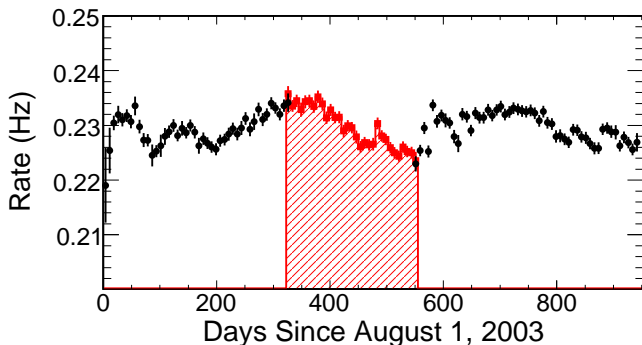


FIG. 4: Muon rates per day as a function of day number from the start of data taking with the complete and magnetized detector after the pre-analysis cuts and analysis cuts 1-4. The shaded area shows the period of reverse field running.

entrance or exit points of a track were required to be less than 50 cm from an outside surface of the detector (“3. Fiducial cut”); and a track must pass a quality cut based on $\chi_{fit}^2/ndf < 1.5$ (4. “fit quality cut”). The χ_{fit}^2/ndf parameter is returned by the Kalman filter [16], which is the track fitting algorithm used in this analysis [8]. The distribution used to select this cut value is shown in Fig. 3 and this cut assures that the track found is a good fit to the track hit points.

In Fig. 4 we show the muon rate (Hz) as a function of day number from the beginning of data taking with the complete and magnetized detector after the pre-analysis cuts and analysis cuts. The fluctuations are consistent with seasonal variations in the cosmic ray muon flux [17].

3. Charge Sign Quality Cuts

For the analysis presented in this paper it is necessary to cleanly identify the charge sign of selected muons and to ensure that systematic uncertainties in this iden-

tification are minimized. This clean selection is achieved by placing charge-sign quality requirements on the reconstructed tracks. There are two components to the charge-sign quality cuts. The first cut assures that the charge sign and momentum returned by the track-fitting algorithm has been well-determined. The second cut minimizes residual systematic uncertainties that remain in the data set after the cuts already described have been applied. To increase the robustness of the result two different approaches to identify a clean sample of events were adopted (2a,2b). Consistent results for the cosmic ray muon charge-sign ratio were obtained with the two different approaches.

- (1) “track quality cut” – the significance of the measured muon charge sign and momentum for a track was required to be $(q/p)/\sigma_{q/p} \geq 2.2$, where q is the charge sign and p is the fit momentum. Here (q/p) is the fit parameter returned by the Kalman filter [16] algorithm used in track-fitting and the error on this fit parameter is $\sigma_{q/p}$. In this analysis we treat the quantity $(q/p)/\sigma_{q/p}$ as positive definite. In Fig. 5 we show N_{μ^+}/N_{μ^-} , the ratio of the number of μ^+ to μ^- , as a function of $(q/p)/\sigma_{q/p}$ after all other cuts have been made since the final two cuts in the analysis are closely correlated. For $(q/p)/\sigma_{q/p} \geq 2.2$, the charge ratio becomes asymptotically flat, suggesting that the charge sign and momentum are well fit. As $(q/p)/\sigma_{q/p}$ tends to zero, the fitter is becoming less reliable at determining the charge sign. For the lowest values of the significance, the fitter picks the two charge signs with equal probability and the measured charge sign ratio tends to unity. Events with low values of the charge sign significance are typically high momentum tracks (> 100 GeV/c) that traverse the detector in such a way as to bend only slightly in the magnetic field. These events have random charge sign identification.

Fig. 5 shows that the DF and DR data sets appear to behave very similarly with respect to the entire suite of charge sign quality cuts. Notwithstanding this similar behavior, there is a clear offset in the charge ratio on the plateau regions where the cuts define the tracks with well-determined charge sign. For the DF data set, $N_{\mu^+}/N_{\mu^-} = 1.40$; for the DR data set, $N_{\mu^+}/N_{\mu^-} = 1.33$. This overall systematic difference is discussed below.

To check the consistency of the analysis, the final cut used was either (2a) or (2b).

- (2a) “MIC” (Minimum Information Cut) analysis – a track was required to have at least 60 planes where the hit information was within 3.5 meters of the detector center; it was also required that the track fitter use the hits from these planes in its determination of (q/p) . Here a ‘plane of hit information’

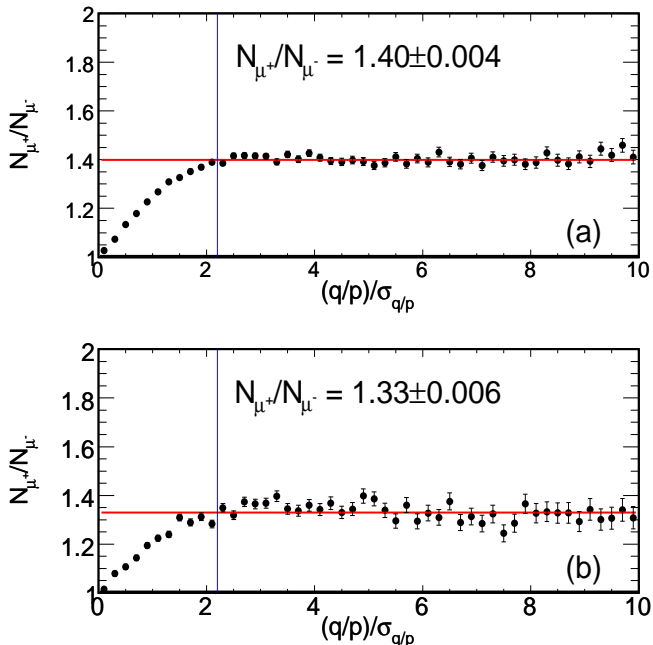


FIG. 5: The N_{μ^+}/N_{μ^-} ratio for reconstructed muon tracks as a function of $(q/p)/\sigma_{q/p}$ after all other cuts. (a) Data Forward (DF) data distribution; (b) Data Reverse (DR) data distribution. As indicated, the cut was chosen at $(q/p)/\sigma_{q/p} > 2.2$ for both data sets, where $(q/p)/\sigma_{q/p}$ becomes asymptotically flat. The figures are labeled with the fits to a constant N_{μ^+}/N_{μ^-} ratio for the cut at $(q/p)/\sigma_{q/p} > 2.2$. The fits are superposed onto the data as horizontal lines.

is defined as a plane containing a strip from which signal is read out on both ends. This cut was motivated by the need for high quality track information to resolve ambiguities in the charge sign determination for events with $p \sim 50$ GeV/c.

The effect of this cut is shown in Fig. 6, where the muon charge ratio, N_{μ^+}/N_{μ^-} is plotted for the (a) DF and (b) DR data sets as a function of fit momentum. In this plot the number of planes of information required where the hits are within a radius of 3.5 m from the detector center has been varied from 0 (no cut) -100 planes. Without the *MIC* cut, there is a large bump in the charge ratio distribution that peaks in the neighborhood of 40 – 50 GeV/c and which decreases as the fraction of the track information in the inner part of the detector, where the field strength is well-characterized, increases. A second feature, which has much poorer statistics, appears near 100 GeV. If these features were real physical effects, then we would not expect them to disappear as the quality of the fit information improved nor would we expect them to become reversed when the field was reversed. But as is clear from Fig. 6, the features do diminish as the number of planes of hit information increases and they do reverse when the field reverses. Further, there is a

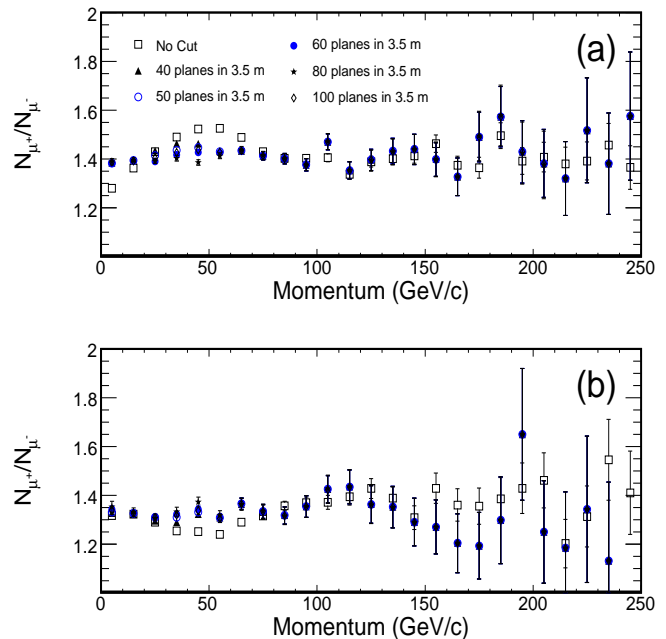


FIG. 6: The muon charge ratio N_{μ^+}/N_{μ^-} for (a) the DF and (b) the DR data sets as a function of fit momentum as the number of planes of track information within 3.5 m of the detector center is varied from zero (no cut) - 100 planes.

large dip at low momenta in the DF data set that is not seen in the DR data set which also becomes negligible as the number of planes of hit information increases. We therefore adopted the *MIC* cut at 60-planes to minimize these systematics. The cut was placed at 60 planes because the addition of more planes of information did not appreciably reduce the systematic error while it does reduce the statistics for the number of events passing the cut.

- (2b) “*BdL*” analysis – a track was required to have an integral field strength of $BdL > 12$ Tesla-meters (Tm), where BdL is a measure of the perpendicular magnetic field B_{perp} traversed by the track. For this analysis a variable BdL was defined as

$$BdL \equiv \int_{beg}^{end} B_{perp}(r) dL, \quad (1)$$

where $B_{perp} = |\vec{B}(r) \times \vec{n}|$ is the component of the magnetic field perpendicular to the track direction \vec{n} at a given point along the track path, r is the distance from the detector center axis, dL is the differential pathlength element along the track, *beg* is the point at which the muon enters the detector and *end* is the point at which it either exits the detector or stops in the detector. For our purposes, the track trajectory was approximated as a straight line running from the start to the end of the track. Since the track length of a long track is 43% in the

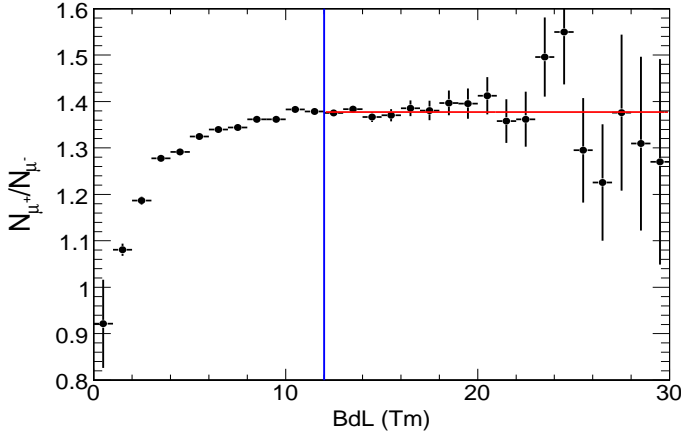


FIG. 7: The charge ratio N_{μ^+}/N_{μ^-} as a function of BdL . The errors shown are statistical. Superposed is the fit to a constant charge ratio N_{μ^+}/N_{μ^-} for $BdL > 12$.

steel, the cut at 12 Tm corresponds to a p_t kick from the magnetic field of 1.5 GeV.

The charge ratio as a function of the variable BdL is shown in Fig. 7. For low values of BdL , the measured charge ratio approaches unity, as expected in the case of random charge determination. As the integrated magnetic field increases, the charge ratio increases to a plateau value where the charge misidentification is highly suppressed. The plateau value is reached at $BdL = 12$ Tm, as shown in Fig. 7. Above this value the charge ratio as function of BdL is consistent with being constant.

The effect of these cuts on the DF and DR data samples is given in Table 1.

As can be seen from Table I, tight cuts are required to minimize systematic errors in charge sign identification for the cosmic muon data sample. Since the Forward (DF) and Reverse (DR) data samples behave similarly with respect to the total suite of cuts, we can use both data sets in subsequent analyses, even though there are overall systematic differences in their N_{μ^+}/N_{μ^-} ratios.

IV. MUON CHARGE RATIO AT THE MINOS FAR DETECTOR

In the sections below we determine the muon charge ratio, N_{μ^+}/N_{μ^-} , as a function of the reconstructed muon momentum, p_{fit} , by using the magnetic field of MINOS.

A. Measurement of the Muon Charge Ratio Underground

In Fig. 8 we show the charge ratio for events with reconstructed tracks that pass all cuts in Table I as a func-

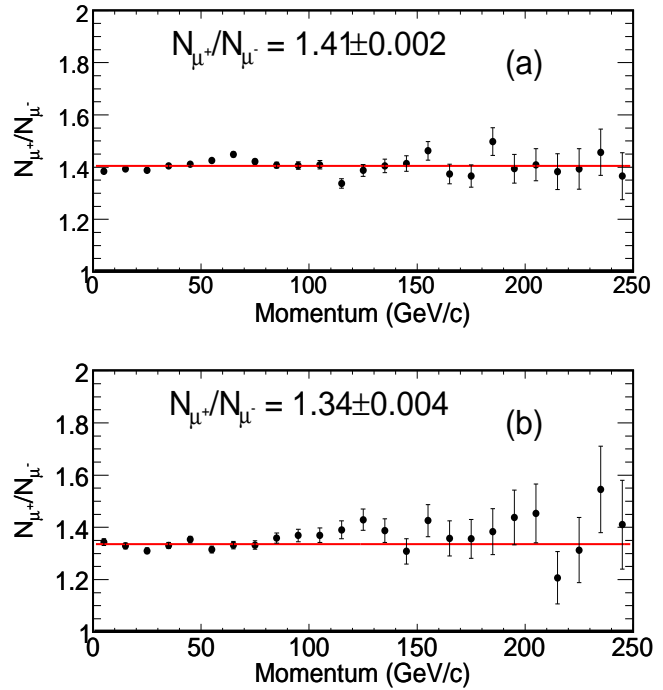


FIG. 8: The charge ratio N_{μ^+}/N_{μ^-} as a function of fit momentum for (a) the DF data set and (b) the DR data set. For this figure, the data set was generated using the *MIC* cut. Superposed on both are the fits to a constant charge ratio N_{μ^+}/N_{μ^-} .

tion of p_{fit} , the reconstructed momentum of the muon. In this and the figures that follow, p_{fit} is labeled “Momentum”. In Fig. 8 the charge ratio is shown separately for (a) the DF and (b) the DR data sets; for these distributions the *MIC* cut was used. Superposed onto the data are fits to a constant charge ratio. Fig. 8 clearly shows the systematic differences in the charge ratio measurements between Forward and Reverse field running.

A method to cancel geometrical acceptance effects and alignment errors is discussed in [18, 19]. If A_1 is the acceptance for μ^+ and A_2 is the acceptance for μ^- in the Forward field direction, then the acceptances in the Reverse field direction are A_1 for μ^- and A_2 for μ^+ . We can thus write two independent equations for the charge ratio in which the geometrical acceptances cancel:

$$r_a = (N_{\mu^+}/t)_{DF}/(N_{\mu^-}/t)_{DR}, \quad (2)$$

and

$$r_b = (N_{\mu^+}/t)_{DR}/(N_{\mu^-}/t)_{DF}, \quad (3)$$

By eliminating the Forward and Reverse live times, t_{DF} and t_{DR} , between the two equations, we obtain a measurement of the mean charge ratio, r , in which both geometrical acceptance and live time biases cancel,

$$r = [r_a \times r_b]^{1/2} = [(N_{\mu^+}/N_{\mu^-})_{DF} \times (N_{\mu^+}/N_{\mu^-})_{DR}]^{1/2}. \quad (4)$$

TABLE I: Summary of the Cuts Applied

	DF ^a	DR ^b
# events before cuts	N=29.0 × 10 ⁶	N=8.9 × 10 ⁶
cut	Fraction Remaining	
No Cuts	1.0	1.0
Pre-Analysis Cuts:		
1. no reconstruction	0.790	0.832
2. multiples	0.733	0.776
3. coil status	0.730	0.772
Analysis Cuts:		
1. 20 plane cut	0.554	0.585
2. 2m track length cut	0.551	0.582
3. fiducial cut	0.534	0.565
4. fit quality cut: $\chi^2_{fitter}/ndf < 1.5$	0.427	0.452
Charge-sign quality cuts		
1. $(q/p)/\sigma_{q/p} \geq 2.2$	0.141	0.147
2a. <i>MIC</i> cut	0.048	0.050
2b. <i>BdL</i> cut	0.033	0.031

^a DF = cosmic data set, forward field

^b DR = cosmic data set, reverse field

Eq. (4) shows that it is the geometrical mean of the two independent charge ratio measurements that corrects for geometrical acceptance.

Another class of systematic uncertainties, those that vary linearly with time, can also be cancelled by careful selection of the data analyzed. If there are systematic effects that depend on live time in a linear way, these systematics can be cancelled by using Forward and Reverse data sets obtained during equal intervals of live time. In this analysis we make two independent measurements of the charge ratio using data sets constructed in this way. We first divide the Reverse data into two sets, DR_1 and DR_2 , each of which has live time equal to $t_{DR}/2$. We then pair DR_1 with DF_1 , a Forward data set also with live time $t_{DR}/2$ which falls at the end of the first period of Forward running (c.f., Fig. 4), in Eq. (4). These data result in one independent measurement of the charge ratio, r_1 ,

$$r_1 = [(N_{\mu^+}/N_{\mu^-})_{DF_1} \times (N_{\mu^+}/N_{\mu^-})_{DR_1}]^{\frac{1}{2}} \quad (5)$$

The second measurement comes from pairing DR_2 with DF_2 , a Forward data set with live time $t_{DR}/2$ which comes at the beginning of the second period of Forward running (c.f., Fig. 4), in Eq. (4). These data result in second independent measurement of the charge ratio, r_2 ,

$$r_2 = [(N_{\mu^+}/N_{\mu^-})_{DF_2} \times (N_{\mu^+}/N_{\mu^-})_{DR_2}]^{\frac{1}{2}} \quad (6)$$

For these measurements, the data sets are all of length $t_{DR}/2$. This analysis relies on systematic errors dominating over statistical errors since the method limits the sample sizes.

In sections §IV B and IV C the analysis just described is applied to the data sets generated with the *MIC* and *BdL* analyses.

B. *MIC* Analysis

In Fig. 9 we show the charge ratio N_{μ^+}/N_{μ^-} for the two data sets r_1 and r_2 as a function of p_{fit} . The two independent measurements of the charge ratio are consistent with one another, which suggests we have significantly reduced the systematics seen in Fig. 8. We have used the data for r_1 and r_2 independently in a fit to a constant charge ratio over the range $0 \leq p_{fit} \leq 150$ (GeV/c). In this fit, each fit momentum bin was assumed to have two independent measurements of the charge ratio. The results of this fit give $N_{\mu^+}/N_{\mu^-} = 1.370 \pm 0.003$ with $\chi^2/ndf = 1.15$ for 29 degrees of freedom. The best fit to a constant charge ratio has been superposed onto the r_1 and r_2 data in Fig. 9 and is labeled r .

In Figs. 10 and 11, we show the charge ratio as a function of zenith angle and azimuth. The analysis for both horizon coordinates follows the analysis for the charge ratio as a function of fit momentum. There is no evidence for an angular dependence of the measured charge ratio.

From Figs. 9, 10, and 11, we find small differences in the charge ratio depending on the parameter used to bin the data. Some of these differences could result from the particular binning chosen for the different parameter plots. To remove differences due to binning, we computed the charge ratios in Eq. (5) and Eq. (6) directly for all data with $p_{fit} < 250$ GeV/c. Using the *MIC* selection in the charge ratio analysis, we find the bin free charge ratio is

$$r = 1.372 \pm 0.003, \quad (7)$$

where the error is statistical. The number of events used in the computation of this ratio are given in Table II.

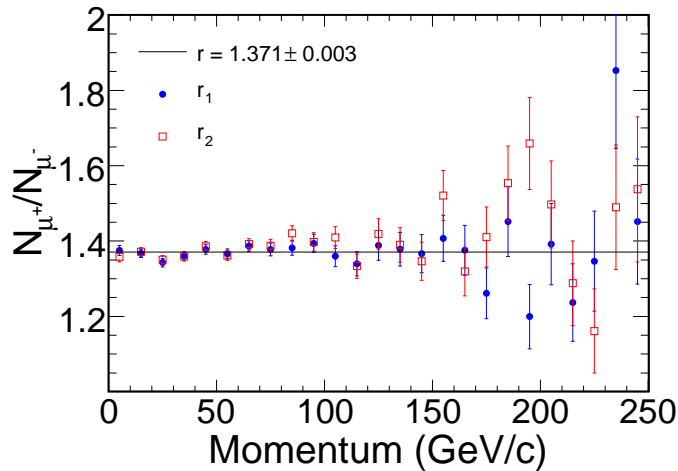


FIG. 9: The charge ratio N_{μ^+}/N_{μ^-} as a function of fit momentum, p_{fit} . For this figure, the data set was generated using the *MIC* cut. The errors shown are statistical. Superposed is the fit to a constant charge ratio N_{μ^+}/N_{μ^-} .

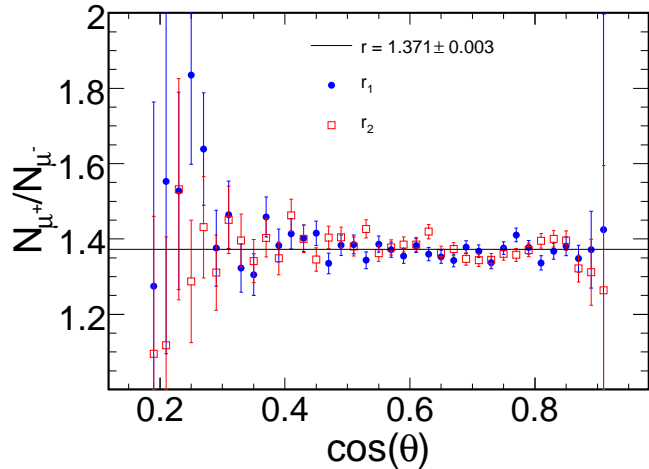


FIG. 10: The charge ratio N_{μ^+}/N_{μ^-} as a function of $\cos\theta$, where θ is the zenith angle. The errors shown are statistical. Superposed is the fit to a constant charge ratio N_{μ^+}/N_{μ^-} .

C. *BdL* Analysis

Using the *BdL* selection in the charge ratio analysis, we find the bin free charge ratio for all data with $p_{fit} < 250$ GeV/c is

$$r = 1.377 \pm 0.004, \quad (8)$$

where the error is statistical. The number of events used in the computation of this ratio are given in Table II.

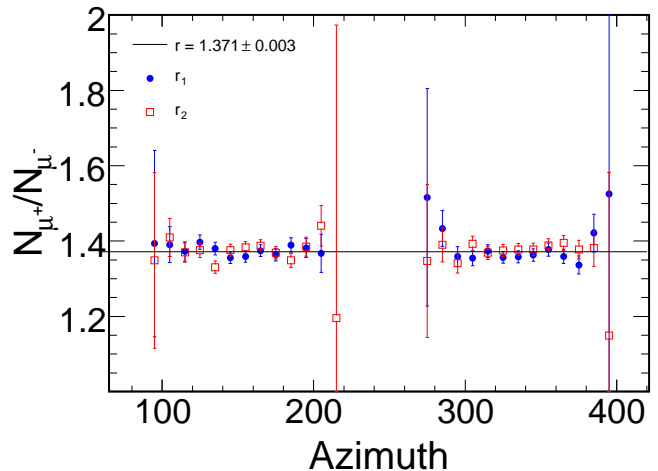


FIG. 11: The charge ratio N_{μ^+}/N_{μ^-} as a function of azimuthal angle ϕ . The errors shown are statistical. The gaps are due to acceptance effects resulting from the planar nature of the detector. Muons with azimuths $< 60^\circ$ have had 360° added to their azimuth so that there is a continuous distribution of muons from the North ($270^\circ - 420^\circ$). Superposed is the fit to a constant charge ratio N_{μ^+}/N_{μ^-} .

TABLE II: Number of Events in *MIC* and *BdL* Samples

	<i>MIC</i>		<i>BdL</i>	
	N_{μ^+}	N_{μ^-}	N_{μ^+}	N_{μ^-}
DF1	132,905	94,792	75,360	52,897
DR1	128,789	96,380	66,581	50,378
DF2	133,382	94,434	73,889	51,126
DR2	125,526	93,802	67,520	51,057

D. Systematic Uncertainties

Using the analysis technique described above many systematic uncertainties cancel. However, there are residual systematic uncertainties which do not cancel. These systematics can be separated into two classes: bias errors and random charge identification errors. Bias errors are those that lead to misidentifications of charge sign and cancel with a high degree of precision when combining forward and reverse field data. The extent to which these errors do not cancel is a measure of the magnitude of these systematics. Randomization errors lead to random misidentifications of charge that do not cancel in Eq. (4). The magnitude of these latter systematic errors have been determined by Monte Carlo simulation. An example of a process that leads to randomization errors is multiple scattering, which can make a straight (high momentum) track appear curved to the track fitter. The charge misidentification of these tracks is independent of charge sign. A second source of randomization error comes from the inclusion of spurious hits in the track fit from bremsstrahlung, cross talk (signal appearing to come from a channel adjacent to the one hit), or

the incorrect assignment of optically summed hits to a plane. Since these hits are likely to fall on either side of the track with equal probability, the incorrect charge sign assignment again occurs with equal probability.

We examine three sources of systematic uncertainties. The first two are bias errors and the third is due to randomization errors.

1. *Combining Forward and Reverse Data.* Here we estimate the residual bias associated with focusing, detector acceptance, the magnetic field map, and misalignments. These cancel in principle when the forward and reverse data sets are combined with Eq. (4). As shown in Fig. 9, the method mostly suppresses the unphysical structures apparent in the charge ratio. We take $(r_a - r_b)/2 = 0.009$, or the residual differences in the charge ratio due to incomplete cancellation of bias systematic errors remaining after the field has been reversed, as a measure of the systematic error associated with our procedure for combining forward and reverse data. The data sets used to calculate r_a and r_b are the same as those used in the computation of r_1 .
2. *Sliding Window.* This bias error determines how stable our determination of the charge ratio remains with respect to time. As described in IV A, systematic errors which grow or decrease linearly in live time can be reduced by combining Forward and Reverse Field data sets in Eq. (4) which have equal live times $t_{DR}/2$. These determine the charge ratios r_1 and r_2 . We have recomputed r_1 and r_2 by successively sliding a window of width $t_{DR}/2$ to alternative times in the first and second periods of Forward Field running. In this way we found a range of ± 0.005 for the charge ratio and this range was adopted as the systematic error.
3. *Random Charge Identification.* Random charge identification errors or ‘randomization’ errors are those that lead to events getting random charge sign assignments. Since the charge ratio N_{μ^+}/N_{μ^-} is greater than one, more positive than negative muons will be misidentified and the measured charge ratio will decrease toward unity. Or equivalently, randomization errors always result in a measurement of the charge ratio that is lower than its true value. Consequently, randomization errors lead to a one-sided (positive) error on the measured charge ratio.

We estimated the magnitude of the randomization systematic error with Monte Carlo simulation and the *BdL* analysis. We use the measurements of the charge ratio with successively tighter cuts on the *BdL* parameter (shown in Fig. 7), a process that systematically reduces the randomization error. Using the trend from Monte Carlo in a χ^2 fit, we estimated the charge ratio without randomization errors. The difference between the fitted value

of the charge ratio without randomization errors and the averaged (MIC/*BdL*) value of the charge ratio is 0.007. We adopt this value for the systematic error due to random charge identification.

Table III summarizes these systematic uncertainties. The total systematic uncertainty was computed as the quadratic sum of individual uncertainties.

TABLE III: Systematic Uncertainties in the Charge Ratio

Source	$(\sigma_{syst})_i$
1. Combining Forward/Reverse	± 0.009
2. Sliding Window	± 0.005
3. Randomization	+0.007
$\sigma_{syst} = \sqrt{\sum_i (\sigma_{syst})_i^2}$	(+0.012, -0.010)

E. Muon Charge Ratio Underground

For the charge ratio underground as measured by MINOS, we take the average of the charge ratio obtained from the *MIC* and *BdL* analyses, and use the systematic uncertainties listed in Table III, to give the muon charge ratio underground:

$$r = 1.374 \pm 0.004 \text{ (stat.)}_{-0.010}^{+0.012} \text{ (sys.)}. \quad (9)$$

V. THE MUON CHARGE RATIO AT THE SURFACE

To infer the muon momentum at the surface from the momentum measured underground requires knowledge of the rock overburden above the MINOS far detector. However, the rock overburden above detector is of non-uniform composition with bands of iron formation embedded in Ely-Greenstone [20]. The topography of the surface above the MINOS far detector is also not level but rather has surface elevations that vary from 630 to 720 m over the angular region of interest [12]. Since the variations in the composition of the rock overburden are not known directly, the technique used here is to normalize the data to a ‘‘world survey’’ of vertical muon intensity data [21]. Thus, it is possible to derive a value of the slant depth for each solid angle bin.

A. Projection back to the Surface

1. Measured Vertical Muon Intensity at the MINOS Far Detector

In this analysis we use events with good charge sign and momentum reconstruction, that is, those events that pass the cuts in Table I up to and including the *MIC* cut.

As seen in Table II, this data set has the largest statistics. The selected events were first separated into bins of equal solid angle, $\Delta\Omega = \Delta \cos(\theta) \times \Delta\phi = 0.02 \times 0.10$ sr. In each solid angle bin j , the vertical muon intensity was computed according to

$$(I_\mu)_j = \frac{1}{T} \frac{mN_j}{(\epsilon_j A_j \Delta\Omega / \cos\theta_j)}, \quad (10)$$

where T is the live-time; N_j is the number of single muons in bin j ; m is a multiplicative factor, assumed independent of slant depth and direction, that accounts for muon multiplicity; $\epsilon_j = \epsilon(\cos\theta_j, \phi_j)$ and $A_j = A(\cos\theta_j, \phi_j)$ are the efficiency and the projected area of the detector, respectively, as a function of zenith and azimuthal angles; and the $\cos(\theta_j)$ factor corrects for the muon intensity zenith angle dependence at the surface to a good approximation in the momentum range relevant here. The intensity is converted to vertical intensity to facilitate comparison with the world survey data. Each measurement of $(I_\mu)_j$ is an independent measurement of the vertical muon intensity in direction $(\cos\theta_j, \phi_j)$.

The efficiency of the far detector, $\epsilon_j = \epsilon(\cos\theta_j, \phi_j)$, for the reconstruction of single muon tracks was computed with Monte Carlo generated muons. We conservatively estimate that uncertainty on our computation of ϵ to be less than a few percent.

The projected area of the MINOS far detector in direction $(\cos\theta_j, \phi_j)$, $A_j = A(\cos\theta_j, \phi_j)$, was computed by first finding the unit vector along this direction, $\hat{\mathbf{n}}_\mu = \hat{\mathbf{n}}_\mu(\cos\theta_j, \phi_j)$, and then defining the normal for each of the ten surfaces of the MINOS far detector, $\hat{\mathbf{n}}_k$, where $k = 1 - 10$. The projected area is then given by

$$A_j = A(\cos\theta_j, \phi_j) = \sum_{k=1}^{10} (\hat{\mathbf{n}}_\mu \cdot \hat{\mathbf{n}}_k) S_k, \quad (11)$$

for all $(\hat{\mathbf{n}}_\mu \cdot \hat{\mathbf{n}}_k) \geq 0$ and where S_k is the area of the k th surface of the MINOS far detector. Our computations show that the total acceptance for the MINOS far detector to single atmospheric muons is $(\epsilon A\Omega) = \sum_j (\epsilon_j A_j \Delta\Omega) = 1.3 \times 10^6$ cm² sr.

To compare our results to those of other underground experiments [11], we make a correction to our measured vertical intensity to account for muon multiplicity, the correction factor m in Eq. (10). Using a day of MINOS far detector data, we find that $m = 1.04$. Since no corrections were made for the lateral distribution of multiple muons over the finite size of the MINOS detector, we conservatively assess an uncertainty of 10% on m .

2. Determination of the MINOS Slant Depth Map for Standard Rock

For each solid angle bin j in direction $(\cos\theta_j, \phi_j)$ we computed a value for the slant depth, X_j , or the column

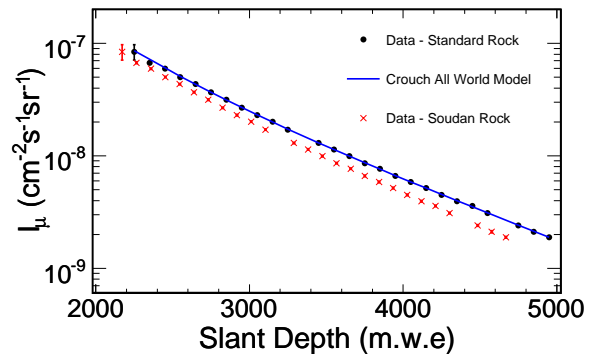


FIG. 12: The vertical muon intensity in the MINOS far detector hall. Shown as solid circles are the vertical intensity data which have been normalized to the Crouch all-world average vertical intensity for standard rock [21]. Overlaid onto the solid circles is the Crouch average. Shown as x's is the vertical intensity for the MINOS far detector hall corrected for Soudan rock.

of rock from the MINOS cavern to the surface in units of m.w.e. (where 1 m.w.e. = 10² g/cm²) by equating our measured vertical muon intensity to Crouch's all-world average vertical muon intensity [21]. This parameterization represents the integral of muons of all energies at the surface that can reach the detector through a rock depth X_j . In particular, we varied X_j until the Crouch parameterization and our measured vertical intensities agreed. Some solid angle bins at the edge of the acceptance had too few events to reliably determine the slant depth; these solid angle bins and their events were removed from further analysis. One solid angle bin located near the zenith and on the edge of the detector acceptance had just enough events for the slant depth of that bin to be calculated. However, the calculated slant depth was several hundred m.w.e. less than the slant depth of neighboring solid angle bins. Given the small acceptance of the bin and the peculiar slant depth derived for it, this solid angle bin and its events were also removed from the analysis.

Since the Crouch parameterization is given in terms of "standard rock", the MINOS slant depth map computed here is in terms of standard rock. In Fig. 12 we show the vertical muon intensity in the range 2000 m.w.e. $\leq X \leq 5000$ m.w.e. made using the MINOS slant depth map with the Crouch parameterization superposed. The two distributions coincide as they must.

3. Vertical Muon Intensity for Soudan Rock

Muons of energy $E_{\mu,0}$ at the Earth's surface lose energy [11] as they traverse a slant depth X through the Soudan rock to the MINOS detector according to

$$-\frac{dE_\mu}{dX} = a(E_\mu) + b(E_\mu)E_\mu, \quad (12)$$

TABLE IV: Rock Parameters

	$\langle Z/A \rangle$	$\langle Z^2/A \rangle$
Standard Rock	0.5	5.5
Soudan Rock	0.5	6.1

where the parameters a and b describe the energy lost by collisional and radiative processes, respectively. Eq. (12) assumes continuous energy loss and does not account for fluctuations [22]. The energy loss parameters for standard rock, (a_s, b_s) , as a function of energy are given in [11]. At the detector, the energy of the muons, E_μ , can approximately be related to $E_{\mu,0}$ by [11]

$$E_{\mu,0} = (E_\mu + a/b)e^{bX} - a/b. \quad (13)$$

To convert the MINOS slant depths for standard rock to Soudan rock, we equate the minimum energy required to reach slant depth X_s of standard rock to the minimum energy required to reach the equivalent slant depth X_M for Soudan rock [23, 24, 25]. If (a_M, b_M) describe the energy loss parameters for the Soudan rock at MINOS, then

$$X_M = \frac{1}{b_M} \ln \left[1 + \left(\frac{a_s}{b_s} \right) \left(\frac{b_M}{a_M} \right) (e^{b_s X_s} - 1) \right]. \quad (14)$$

The values of the energy loss parameters a and b depend on the average composition of the rock [25]. For the collisional term,

$$a_M = a_s \left\langle \frac{Z_M}{A_M} \right\rangle \left\langle \frac{Z_s}{A_s} \right\rangle^{-1},$$

and for the radiative term

$$b_M = b_s \left\langle \frac{Z_M^2}{A_M} \right\rangle \left\langle \frac{Z_s^2}{A_s} \right\rangle^{-1},$$

where Z is the atomic number and A is the atomic mass. The parameters for standard rock and the Ely-Greenstone rock at the Soudan Underground Laboratory [20] are shown in Table IV.

The vertical intensity using the Soudan rock map is shown in Fig. 12. Since $\langle Z_M^2/A_M \rangle$ is larger for Soudan rock than for standard rock, a muon will lose more energy traversing an equivalent column of Soudan rock and therefore the vertical intensity at MINOS will have a steeper slope, as seen. In Fig. 13 we use the MINOS slant depth map to plot the charge ratio as a function of the slant depth. Fig. 13 shows that the charge ratio has little dependence on slant depth.

4. Projection back to the Surface

The muon energy underground is obtained from the reconstructed momentum. To project the reconstructed muon energies underground, $E_\mu = cp_{fit}$, back to the surface, we used Eq. (13) with Soudan rock parameters and

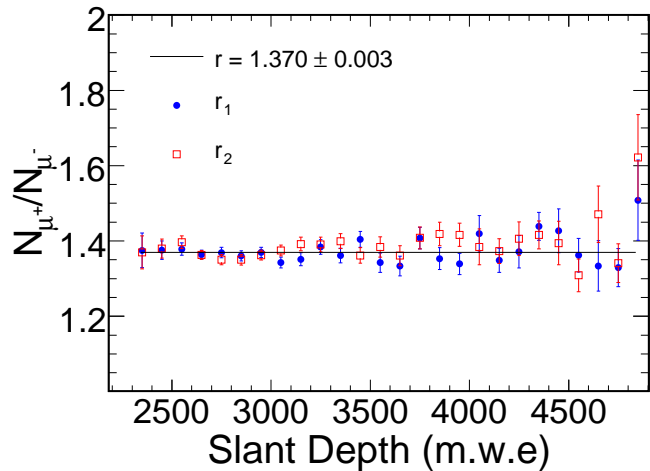


FIG. 13: The charge ratio N_{μ^+}/N_{μ^-} as a function of slant depth in Soudan rock. The errors shown are statistical. Superposed is the fit to a constant charge ratio N_{μ^+}/N_{μ^-} .

the MINOS rock map. In these projections, we assumed that the Soudan energy loss parameters varied with energy in a manner similar to the energy loss parameters for standard rock in [11]. In Fig. 14 we show the result of this projection for three slant depth bins used to compute the vertical intensity in Fig. 12. This figure shows the distributions of surface muon energies, $E_{\mu,0}$, for these three bins, as well as the median energy, $\langle E_{\mu,0} \rangle_{med}$, for each distribution. The width of the slant depth bins is 100 m.w.e. and this width is the dominant contributor to the width of the surface energy distributions shown. The expected increase of surface energy with increasing slant depth is clearly evident.

B. The Energy Dependence of the Muon Charge Ratio at the Surface

Using Eq. (13) we projected the muons from the *MIC* analysis back to the surface. For each successfully reconstructed muon underground, we use its p_{fit} value, its slant depth X , and the Soudan values of (a_M, b_M) to obtain the surface energy $E_{\mu,0}$. In these projections, we assumed that the Soudan energy loss parameters were independent of charge sign and they varied with energy in a manner similar to the energy loss parameters for standard rock in [11].

Once projected back to the surface, we sorted the muons into bins of width 0.25 TeV and then computed the charge ratio. The results are shown in Fig. 15, where the charge ratio N_{μ^+}/N_{μ^-} is plotted as a function of surface muon energy $E_{\mu,0}$. In Table V we give the charge ratio data in each energy bin, as well as the weighted mean.

We have performed 1-parameter and 2-parameter fits

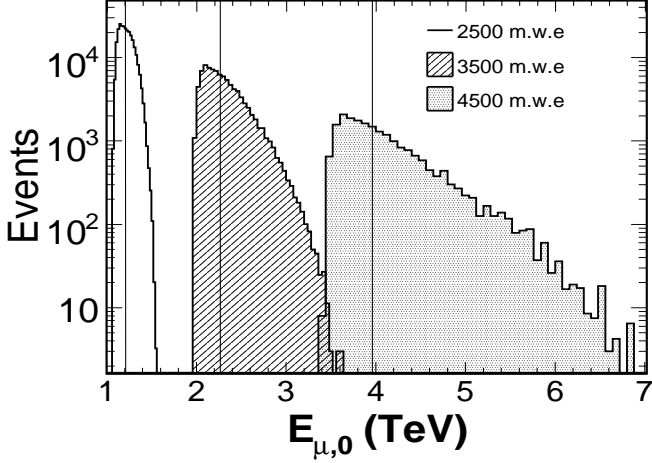


FIG. 14: The distribution of muon energies projected back to the surface for three slant depth bins of width 100 m.w.e used in the computation of the vertical intensity in Fig. 12. These projections were made with Eq. (13) and Soudan rock parameters. The median value of the muon energy $\langle E_{\mu,0} \rangle_{med}$ on the surface for these three bins is shown.

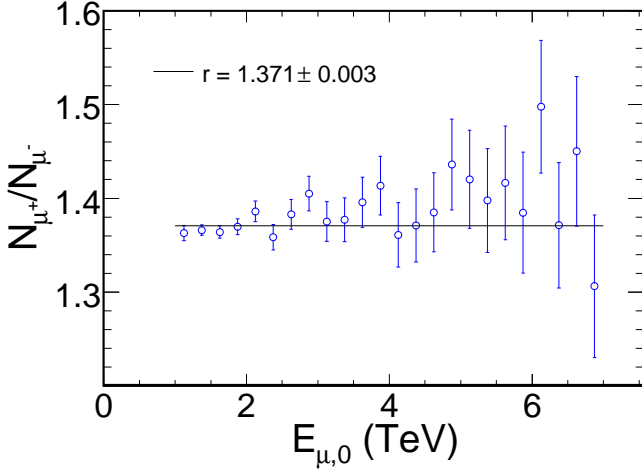


FIG. 15: The muon charge ratio N_{μ^+}/N_{μ^-} at the Earth's surface. The errors shown are statistical.

to the data in Table V over the surface muon energy range $1.0 \text{ TeV} < E_{\mu,0} < 7.0 \text{ TeV}$. A fit to a constant charge ratio gives

$$N_{\mu^+}/N_{\mu^-} = 1.371 \pm 0.003 \text{ (stat.)}_{-0.010}^{+0.012} \text{ (sys.)}, \quad (15)$$

with $\chi^2/ndf = 63.2/67$. The data are consistent with a charge ratio that is independent of energy.

The 2-parameter linear fit gives

$$N_{\mu^+}/N_{\mu^-} = (1.354 \pm 0.007) + (0.85 \pm 0.33) \times 10^{-2} E_{\mu,0}, \quad (16)$$

where $E_{\mu,0}$ is in TeV and $\chi^2/ndf = 56.6/66$.

TABLE V: Charge Ratio at the Surface

$E_{\mu,0}$ (TeV)	r
1.00 – 1.25	1.363 ± 0.008
1.25 – 1.50	1.366 ± 0.006
1.50 – 1.75	1.364 ± 0.007
1.75 – 2.00	1.370 ± 0.009
2.00 – 2.25	1.386 ± 0.011
2.25 – 2.50	1.359 ± 0.014
2.50 – 2.75	1.383 ± 0.016
2.75 – 3.00	1.405 ± 0.019
3.00 – 3.25	1.375 ± 0.021
3.25 – 3.50	1.377 ± 0.023
3.50 – 3.75	1.396 ± 0.027
3.75 – 4.00	1.413 ± 0.031
4.00 – 4.25	1.361 ± 0.034
4.25 – 4.50	1.371 ± 0.039
4.50 – 4.75	1.385 ± 0.042
4.75 – 5.00	1.436 ± 0.048
5.00 – 5.25	1.420 ± 0.052
5.25 – 5.50	1.398 ± 0.055
5.50 – 5.75	1.417 ± 0.061
5.75 – 6.00	1.385 ± 0.065
6.00 – 6.25	1.498 ± 0.071
6.25 – 6.50	1.371 ± 0.067
6.50 – 6.75	1.450 ± 0.080
6.75 – 7.00	1.306 ± 0.076
$\langle r \rangle$	1.371 ± 0.003

There are two contributions to the systematic error on the slope: uncertainties in the calculation of the energy scale $E_{\mu,0}$ and errors on the determination of the slope due to randomization. Errors in the energy scale are mostly due to uncertainties in the rock map; these errors are estimated to be $\sim 10\%$. Calculations show that errors in the surface muon energies resulting from systematic uncertainties in the slant depth map of this order are 15-20% at 2100 m.w.e. and 25% at 4000 m.w.e. In a second test, the Soudan 2 slant depth map [12] was substituted for the MINOS slant depth map and the surface energies recomputed. The differences in the surface energies determined with these two maps are again approximately 20%. We therefore estimate the systematic error on the energy scale to be $\pm 20\%$. The uncertainty in the energy scale does not affect the significance of the slope.

Systematics due to randomization do affect the significance of the slope determination. For long track lengths, the tracks are better reconstructed, the charge misidentification is smaller, and the measured charge ratio systematically rises. Thus randomization can mimic and cover up a rising dependency of the muon charge ratio on muon surface energy. To estimate the size of this effect, we have separated the data into six subsets with BdL values from 10 Tm to 15 Tm. As expected, we found these data sets to have different values of the charge ratio due to different but fixed amounts of randomization at the level of approximately 2%. In contrast, the values for the slope of the charge ratio versus surface energy were similar. This randomization-free value for the slope parameter

was 30% smaller than the value from the two parameter fit. We take this difference to be the systematic error on the slope,

$$\text{slope} = 0.85 \pm 0.33(\text{stat}) \pm 0.26(\text{syst}) \times 10^{-2} \text{ TeV}^{-1} \quad (17)$$

Adding the errors in quadrature shows that the slope differs from zero by two sigma. An alternative fit using a linear dependence on $\log E_\mu$ yields a similar result.

VI. DISCUSSION

In order to obtain the charge ratio results shown in Fig. 15, each muon in our sample was projected back to the surface with Eq. (13) using the Soudan energy loss parameters (a_M, b_M) for both μ^+ and μ^- . A theoretical complication to this procedure is the possibility that the energy loss parameters a and b are different for the two charges. For ionization losses, it was pointed out by Fermi [26] that the electrons in matter would introduce small differences in energy loss. Calculations by Jackson and McCarthy [27] confirmed that negative particles lose energy at a slower rate, with the difference dropping from tens of percent at MeV energies to about 0.3% in the GeV range. These calculations were subsequently verified experimentally both at MeV energies [28, 29, 30] and in the GeV range [31]. The approximations used in [27], however, break down when going to even higher energies and so more exact numerical methods are needed. A calculation at TeV energies can be found in Jackson [32] that shows a small 0.15% increase in the ionization loss for μ^+ over μ^- . For radiative energy loss, which involves the parameter b , the difference between μ^+ and μ^- is much smaller and falls with energy [33]. In the extrapolation used to obtain the results below, we assumed the same energy loss function for both charges.

The projections of our data back to the surface, plotted in Fig. 15 as a function of surface energy, yield a charge ratio significantly higher at few TeV than those measured by others at surface energies below 300 GeV [2, 3]. This rise in the charge ratio at TeV energies is, however, expected as the result of the increasing contribution of kaons to the cosmic ray muon flux at these energies and the greater likelihood for kaons to decay to μ^+ than for pions to decay to μ^+ [13].

We use a qualitative model of the charge ratio to show that the rise in the charge ratio at TeV energies seen in Fig. 15 is consistent with this expectation. Gaisser [13] and Gaisser and Stanev [11] give an expression for the muon intensity at the surface as a function of the muon energy and zenith angle. It has contributions from both pion and kaon decay and it comes from folding the measured spectrum of cosmic ray primaries with the kinematics of pion and kaon decay. In our model we assume this expression holds independently for both μ^+ and μ^- . In addition, this model assumes that charm production can be neglected and that pion and kaon interaction lengths are independent of charge at these energies. Let f_{π^+} be

the fraction of all pion decays with a detected muon that is positive. Then $(1 - f_{\pi^+})$ is the fraction of all pion decays with a detected muon that is negative. Similarly, let f_{K^+} be the fraction of all kaon decays with a detected muon that is positive and $(1 - f_{K^+})$ be the fraction of all kaon decays with a detected muon that is negative. The muon charge ratio N_{μ^+}/N_{μ^-} can then be written

$$\frac{N_{\mu^+}}{N_{\mu^-}} = \left[\frac{f_{\pi^+}}{1 + \frac{1.1E_{\mu^+} \cos \theta}{115 \text{ GeV}}} + \frac{0.054f_{K^+}}{1 + \frac{1.1E_{\mu^+} \cos \theta}{850 \text{ GeV}}} \right] / \left[\frac{(1 - f_{\pi^+})}{1 + \frac{1.1E_{\mu^-} \cos \theta}{115 \text{ GeV}}} + \frac{0.054(1 - f_{K^+})}{1 + \frac{1.1E_{\mu^-} \cos \theta}{850 \text{ GeV}}} \right] \quad (18)$$

The simplest assumption to make in this model is that f_{π^+} and f_{K^+} are independent of energy. Although this assumption neglects many physical processes that may play a role at these energies, it is an assumption that is a reasonable choice to qualitatively describe our results: a rise in the charge ratio from a plateau at a few hundred MeV to a second higher plateau at a few TeV. This rise has already been seen in the results from the CORT cosmic ray Monte Carlo [1] and the models of Lipari [34]. Below we test this simple model with the MINOS data.

We used Eq. (18) with the MINOS data set and the L3+C data set [3] to find the values of f_{π^+} and f_{K^+} that best describe these two data sets. We used these data because they have the angular information needed for the fit. We found the best fit values for f_{π^+} and f_{K^+} with a grid search over (f_{π^+}, f_{K^+}) parameter space. At each point in the space a χ^2 statistic compared the mean charge ratio weighted by solid angle with the model predictions represented by Eq. (18). The charge ratio values in each bin had uncertainties given by the quadratic sum of the statistical and systematic errors. The χ^2 minimum is found at $f_{\pi^+} = 0.55$ and $f_{K^+} = 0.67$, with $\chi^2/ndf \simeq 1$. In Fig. 16, we have superposed this ‘ πK ’ model onto the MINOS and L3+C data sets [3]. The qualitative results of the model are that the observed rise in the muon charge ratio can be explained by the increasing importance of kaon decays to the muon charge ratio as the energy increases from 0.3 – 1 TeV and that values of f_{π^+} and f_{K^+} that are independent of energy are sufficient to describe the MINOS and L3+C data.

Fig. 17 shows the πK model superposed onto a compilation of data from the literature, as well as the MINOS and L3+C data. The additional data also support the results of this simple model.

VII. SUMMARY

The analysis presented here can be separated into three parts. First, we computed the muon charge ratio underground. To minimize residual systematic errors, we combined data with both forward and reversed magnetic field running configurations. When combined, two independent analyses (MIC/BdL) give a muon charge ratio

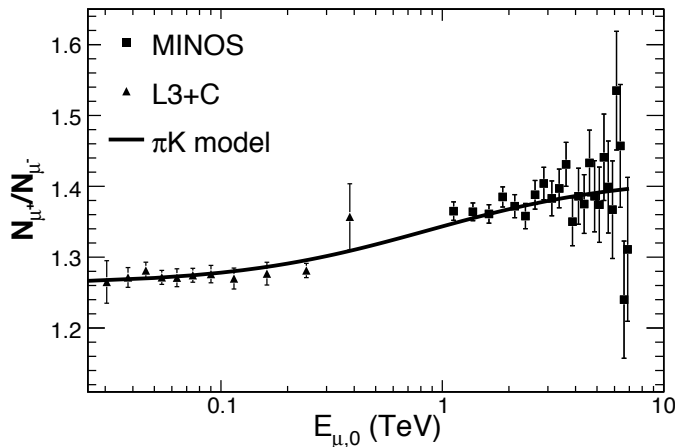


FIG. 16: The πK model discussed in the text superposed onto the MINOS and L3+C data sets. The MINOS charge ratio data are from Table V with a systematic error of ± 0.011 that has been added in quadrature to the statistical error for each data point. The L3+C data are taken from [3].

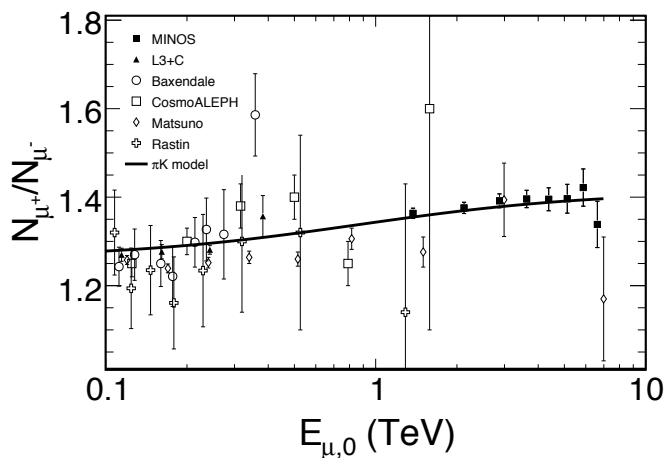


FIG. 17: A compilation of muon charge ratio data from 0.1 to 7 TeV. The MINOS data have been taken from Table V. Other data: L3+C [3], Baxendale [35], CosmoALEPH [36], Matsuno [18], and Rastin [37]. The πK model is superposed.

as measured underground of:

$$N_{\mu^+}/N_{\mu^-} = 1.374 \pm 0.004 \text{ (stat.)}_{-0.010}^{+0.012} \text{ (sys.)}.$$

Second, using a map of the Soudan rock overburden, the muon momenta were corrected to their corresponding values at the surface, spanning the energy range from 1 to 7 TeV. Within this range of energies at the surface, the MINOS data are consistent with the charge ratio being energy independent at the two standard deviation level. The charge ratio as measured by MINOS is significantly higher than measurements by other experiments at surface energies below 300 GeV. Finally, we used MINOS and L3+C data in a simple model that attributes the rise in the charge ratio with energy to the increasing contribution of kaon decays. Fitting the data to the model gives results that are consistent with this picture.

Acknowledgements

This work was supported by the U.S. Department of Energy, the U.S. National Science Foundation, the U.K. Particle Physics and Astronomy Research Council, the State and University of Minnesota, the Office of Special Accounts for Research Grants of the University of Athens, Greece, FAPESP (Rundacao de Amparo a Pesquisa do Estado de Sao Paulo), CNPq (Conselho Nacional de Desenvolvimento Cientifico e Tecnolico) in Brazil, and the computational resources of the AVIDD cluster at Indiana University. We gratefully acknowledge the Minnesota Department of Natural Resources for their assistance and for allowing us access to the facilities of the Soudan Underground Mine State Park. We also thank the crew of the Soudan Underground Physics laboratory for their tireless work in building and operating the MINOS detector. We acknowledge G. Bodwin of Argonne for useful theoretical discussions.

[1] G. Fiorentini, V. A. Naumov, and F. L. Villante, *Phys. Lett. B* **510**, 173 (2001), hep-ph/0103322.
 [2] T. Hebbeker and C. Timmermans, *Astropart. Phys.* **18**, 107 (2002), hep-ph/0102042.
 [3] P. Achard et al. (L3+C), *Phys. Lett. B* **598**, 15 (2004), hep-ph/0408114.
 [4] T. Sanuki et al., in *Proceedings of the 29th International Cosmic Ray Conference (ICRC)*, Pune, India, 2005, edited by B. S. Acharya et al. (Tata Institute of Fundamental Research, Mumbai, 2005), vol. 9, p. 139.
 [5] G. D. Barr, T. K. Gaisser, P. Lipari, S. Robbins, and T. Stanev, *Phys. Rev. D* **70**, 023006 (2004).

[6] B. J. Rebel, Ph.D. thesis, Indiana University (2004).
 [7] E. B. Beall, Ph.D. thesis, University of Minnesota (2005).
 [8] D. G. Michael et al., *Nucl. Instrum. Methods Phys. Res. Sect. B* (2006), to be submitted.
 [9] P. Adamson et al. (MINOS), *Phys. Rev. D* **73**, 072002 (2006).
 [10] P. Adamson et al. (MINOS Collaboration), *MINOS Technical Design Report*, Fermilab note MINOS-doc-337 (1998).
 [11] W. Yao et al. (Particle Data Group), *J. Phys. G* **33**, 1 (2006), see T.K. Gaisser and T. Stanev, *24. Cosmic Rays*, p. 245.

- [12] S. M. S. Kasahara, Ph.D. thesis, University of Minnesota (1997).
- [13] T. K. Gaisser, *Cosmic Rays and Particle Physics* (Cambridge University Press, 1990).
- [14] A. M. Hawthorne, Ph.D. Thesis, Indiana University (1997).
- [15] A. Blake, Ph.D. thesis, Cambridge University (2005).
- [16] R. Fruhwirth, Nucl. Instrum. Methods Phys. Res. Sect. A **262**, 444 (1997).
- [17] M. Ambrosio et al. (MACRO), *Astropart. Phys.* **7**, 109 (1997).
- [18] S. Matsuno et al., *Phys. Rev. D* **29**, 1 (1984).
- [19] T. Fields, Fermilab note MINOS-doc-1483 (2006).
- [20] K. Ruddick, Fermilab note MINOS-doc-210 (1996).
- [21] M. Crouch, in *Proceedings of the 20th International Cosmic Ray Conference (ICRC)*, Moscow, USSR, 1987, edited by V. Kozyarivsky et al. (Nauka, USSR, 1987), vol. 6, p. 165.
- [22] P. Lipari and T. Stanev, *Phys. Rev. D* **44**, 3543 (1991).
- [23] B. S. Meyer et al., *Phys. Rev. D* **1**, 2229 (1970).
- [24] M. G. K. Menon and P. V. Ramana Murthy, in *Progress in Elementary Particles and Cosmic Ray Physics* (North-Holland, Amsterdam, 1967), vol. 9, p. 190.
- [25] D. DeMuth, Ph.D. thesis, University of Minnesota (1999).
- [26] E. Fermi, Letter to W. H. Barkas (1953).
- [27] J. D. Jackson and R. L. McCarthy, *Phys. Rev. B* **6**, 4131 (1972).
- [28] F. M. Smith, W. Birnbaum, and W. H. Barkas, *Phys. Rev.* **91**, 765 (1953).
- [29] W. H. Barkas, W. Birnbaum, and F. M. Smith, *Phys. Rev.* **101**, 778 (1956).
- [30] M. Agnello et al., *Phys. Rev. Lett.* **74**, 371 (1995).
- [31] A. R. Clark et al., *Phys. Lett. B* **41**, 229 (1972).
- [32] J. D. Jackson, *Phys. Rev. D* **59**, 017301 (1998).
- [33] R. N. Lee et al., *Phys. Rev. A* **69**, 022708 (2004).
- [34] P. Lipari, *Astropart. Phys.* **1**, 195 (1993).
- [35] J. M. Baxendale, C. J. Hume, and M. G. Thompson, *J. Phys. G* **1**, 781 (1975).
- [36] D. Zimmermann et al. (CosmoALEPH), *Nucl. Instrum. Methods Phys. Res. Sect. A* **525**, 141 (2004).
- [37] B. C. Rastin, *J. Phys. G* **10**, 1629 (1984).